ORIGINAL PAPER

Pre-stabilized reduced graphene oxide by ammonia as carrier for Ni(OH)$_2$ with excellent electrochemical property

J. L. Zhang · H. D. Liu · L. H. Huang · S. Z. Tan ·
W. J. Mai · X. Cai

Abstract An advanced electrochemical pseudocapacitor material based on reduced graphene oxide and nickel hydroxide (rGO&Ni(OH)$_2$) was prepared by an easy process where ammonia acted as a pre-stabilizer that could be easily removed. The results showed that the agglomeration and re-stacking of rGO could be effectively prevented, resulting in few-layer rGO nanosheet with high specific surface area of 891.22 m^2/g which could supply large available area for loading nanoparticle. After the incorporation of Ni(OH)$_2$ nanoparticle, the rGO&Ni(OH)$_2$ composite owned excellent electrochemical performance thanks to effective prevention of agglomeration and re-stacking of rGO with large size of the sp^2 domain, no residual of pre-stabilizer of ammonia, and tight contact between rGO and Ni(OH)$_2$. Specifically, the rGO&Ni(OH)$_2$ electrode exhibited excellent stability at scan rates from 100 to 300 mV/s. A high specific capacitance of 1,008 F/g was obtained at high current density of 42 A/g in 6 mol/L KOH aqueous electrolyte, and the specific capacitance demonstrated good rate capability. Moreover, rGO&Ni(OH)$_2$ electrode showed a long cycle life, retaining 74 % specific capacitance after 2,000 cycles at current density of 6 A/g. The advantages of easy process and excellent electrochemical property suggested great potential application of rGO&Ni(OH)$_2$ in supercapacitors.

J. L. Zhang · H. D. Liu · L. H. Huang · S. Z. Tan (✉)
Department of Chemistry, Jinan University, Guangzhou 510632,
People's Republic of China
e-mail: tanshaozao@163.com

W. J. Mai
Department of Physics, Jinan University, Guangzhou 510632,
People's Republic of China

X. Cai (✉)
Department of Light Chemical Engineering, Guangdong
Polytechnic, Foshan 528041, People's Republic of China
e-mail: cecaixiang@163.com

Introduction

Energy storage devices (ESDs), with highly efficient, low-cost, flexible, safe and environment-friendly properties, are importantly significant to solve the problems of limited reserves of fossil fuels, climate changes, energy security concerns, and efficient storages of various energy sources. Among many emerging ESDs, supercapacitors (SCs), also known as electrochemical capacitors or ultracapacitors, are projected to be the best potential candidate and have consequently attracted much considerable attention, by virtue of the higher energy density than that of conventional dielectric capacitors, higher power density than that of batteries, long cycle life, and low maintenance requirement [1–8]. To date, SCs have found extensive applications, including portable consumer electronics, power and memory back-up systems, industrial power, mobile electrical systems, etc. [1, 8–10]. According to the energy storage mechanism, SCs could be divided into two types: electrical double layer capacitors (EDLCs), where capacitance results from the charges electrostatically absorbed and accumulated at the electrode/electrolyte interface, and pseudocapacitors, where energy is stored through redox reaction on the surface of electrode material [11]. Compared with that of conventional EDLCs, the energy density of pseudocapacitors associated with Faradaic reaction is substantially larger by at least one order of magnitude, which has drawn an increasing interest in developing the applications of pseudocapacitors [12–18].

The key component of SCs is electrode materials. They are usually carbon materials for EDLCs while they

are often conducting polymers, transition metal oxides, or transition metal hydroxides for pseudocapacitors, including activated carbon [19], carbon nanotube [20], graphene [21, 22], RuO_x [23], CoO_x [24], NiO_x [25], FeO_x [26], MnO_x [27], $Ni(OH)_2$ [28], polyaniline [29], etc. However, these materials have some lethal defects to lower the performances of SCs, such as limit of energy storage mechanism for carbon material [30], poor electrical conductivity for transition metal oxide or transition metal hydroxide [14], and poor cycling performance for conducting polymer because of the degradation caused by the volume change during the repeated charg-discharge process [31, 32]. In order to overcome these weaknesses and improve the overall performances of SCs, different kinds of strategies have been proposed and have achieved much success. For instance, transition metal oxides, transition metal hydroxides [2, 15, 33, 34], and conducting polymers [29, 35, 36] are incorporated with carbon-based materials. Ji et al. [37] prepared nanoporous $Ni(OH)_2$ thin film on 3D ultrathin-graphene foam via a hydrothermal reaction. Shahid et al. [38] synthesized ultrathin nanoflakes of $Ni(OH)_2$ onto multi-walled carbon nanotubes by chemical precipitation method. Moreover, Chen et al. [39] prepared hybrid $Co_xNi_{1-x}(OH)_2$ nanosheets via microwave-assisted synthetic route. Even so, some key issues still exist. On one hand, the electrochemical performance is usually poor, and especially, the capacitance decay is obvious when electrode materials are applied at high current density or scan rate. On the other hand, most of these strategies require complicated methods or equipments to prepare electrode materials with special structures, like 3D hierarchical porous structures or core-shell structures [14, 15, 29, 40]. Either of these two aspects will limit the extensive applications of SCs.

For solving this predicament, in this paper, we proposed an advanced electrochemical pseudocapacitor material containing reduced graphene oxide and nickel hydroxide ($rGO\&Ni(OH)_2$). The rGO was pre-stabilized by ammonia (NH_3) released from the decomposition of hexamethylenetetramine (($CH_2)_6N_4$) under the condition of heating, and the pre-stabilized rGO was served as carrier for $Ni(OH)_2$. Unlike other stabilizers or modifiers, the pre-stabilizer of NH_3 could effectively protect rGO from agglomeration and re-stacking and could be easily removed. Such obtained few-layer rGO nanosheet exhibited high specific surface area of 891.22 m^2/g, which could provide many available areas for loading nanoparticle. More importantly, after the combination of $Ni(OH)_2$ nanoparticle, the $rGO\&Ni(OH)_2$ composite owned excellent electrochemical property thanks to effective prevention of agglomeration and re-stacking of rGO with large size of the sp^2 domain, no residual of

pre-stabilizer of ammonia, and tight contact between rGO and $Ni(OH)_2$, including high capacitance, good rate capability, excellent stability, long cycle life, etc. The advantages combining facile process and excellent electrochemical performance suggested great potential application of $rGO\&Ni(OH)_2$ in SCs.

Experimental

Materials

Graphite powder (spectral pure) was purchased from Sinopharm Chemical Reagent Co., Ltd. Nickel nitrate hexahydrate ($Ni(NO_3)_2\cdot6H_2O$) was purchased from Jinhuada Chemical Reagent Co., Ltd (Guangzhou, China). Hexamethylenetetramine (($CH_2)_6N_4$) was supplied by Aladdin Reagent Inc (Shanghai, China). Hydrazine hydrate (80 %) was supplied by Fuyu Chemical Reagent Co., Ltd (Tianjin, China). All other reagents and solvents were obtained from commercial suppliers. All aqueous solutions were prepared with ultrapure water (>18MΩ) from a Milli-Q Plus system (Millipore).

Synthesis of rGO and $rGO\&Ni(OH)_2$

Graphene oxide (GO) was prepared by oxidizing natural graphite powder based on a modified Hummers method as originally presented by Kovtyukhova and colleagues [41, 42]. Of as-prepared GO, 0.2 g was dispersed in 200 mL deionized water with the help of ultrasonication. Then, 0.5607 g of ($CH_2)_6N_4$ was added in and the solution was ultrasonicated for 0.5 h. Afterwards, the mixture was placed still in a water bath at 90 °C for 14 h. The resulting product was washed with deionized water and dispersed again in 200 mL deionized water, orderly. 5 g of nickel (II) nitrate hexahydrate was then added into the above solution and the solution was ultrasonicated for 0.5 h. After that, 20 mL 80 % hydrazine hydrate was added in and the mixture was reacted at 95 °C for 2 h. The obtained product was washed with deionized water and then freeze-dried. Such acquired powder was designated as $rGO\&Ni(OH)_2$. Similarly, rGO was prepared according to the same method as described above without the addition of nickel (II) nitrate hexahydrate.

Characterizations

X-ray diffraction (XRD) patterns were taken by a Rigaku D/max 2500v/pc X-ray diffractometer using Cu K_α radiation (K_α=0.15405 nm) within a 2θ range of 5.0–80.0° at a scanning rate of 4.0°/min. A voltage of 36 kV and a current of

20 mA were applied. Fourier transform infrared (FTIR) spectra between 400 and 4,000 cm^{-1} were obtained on a Nicolet 6700 spectrometer. Raman spectra were obtained on a Renishaw RM2000 Raman spectrometer with incident laser light of 514.5 nm. X-ray photoelectron spectroscopy (XPS) spectrum was recorded by an ESCALAB 250 XPS (Thermo-VG Scientific). The chemical compositions of samples were analyzed by energy dispersive X-ray spectrometer (EDX) (Oxford ISIS-300). Atomic force microscopy (AFM) images were observed by a Benyuan CSPM5500 atomic force microscope on a flat mica substrate. Field emission scanning electron microscopy (FESEM) images were performed on ZEISS field emission scanning electron microscope; the samples were coated with a thin layer of gold before analysis. Transmission electron microscopy (TEM) images were observed by using a JEOL JEM-2100F transmission electron microscope. The Brunauer-Emmett-Teller (BET) surface area was determined from nitrogen adsorption and desorption isotherm data obtained at 77 K with a constant-volume adsorption apparatus (Mmk-TriStar3000).

Electrochemical measurements

The fabrication of working electrode was carried out as follows. The electroactive material, carbon black, and polytetrafluoroethylene were mixed with ethanol in a mass ratio of 75:15:10. The resulting slurry was pressed onto the nickel foam substrate (1 cm×1 cm) and then the substrate was subsequently dried at 80 °C for 24 h. The mass of electroactive material in each electrode was approximately 1 mg. Electrochemical measurements were done in a three-electrode setup: nickel foam coated with electroactive material, platinum electrode, and saturated calomel electrode (SCE) were acted as the working electrode, counter electrode, and reference electrode, respectively. The measurements were carried out in a 6 mol/L KOH aqueous electrolyte at room temperature. Cyclic voltammetry (CV) test, galvanostatic charge and discharge (GCD) curve, and electrochemical impedance spectroscopy (EIS) measurement were measured by an IVIUMSTAT electrochemical workstation (Holland). Therein, the CV test was recorded between 0 and 0.45 V (vs. SCE) at different scan rates; GCD curve was measured in the potential range from −0.05 to 0.40 V (vs. SCE) at different current densities; and EIS measurement was carried out at a frequency range from 0.1 to 10^4 Hz with potential amplitude of 10 mV.

Results and discussion

Structure and chemical composition

Figure 1 shows the XRD patterns of GO, rGO, and rGO&Ni(OH)$_2$. For GO, the peak of graphite at 2θ=26.4°

could not be observed. Instead, a new peak centered at 2θ= 9.3° was appeared which was corresponded with the (002) interlayer spacing of 0.950 nm, and the low XRD signal-to-noise ratio indicated the poor crystallinity of sample. These results might be due to high degree of exfoliation and disordered structure of GO after oxidation from graphite. In the XRD pattern of rGO, the peak at 2θ=9.3° was disappeared, which was due to the removal of oxygen-containing functional groups after GO was partially reduced, resulting in the decrease of the interspace distance. Generally speaking, due to the Van der Waals force that often caused the agglomeration or re-stacking of graphene, a peak around 2θ=25° could be obviously observed after reduction process. For rGO, the peak around 2θ=25° was quite flat and broad, demonstrating that the agglomeration and re-stacking phenomenon of the obtained rGO was not visible. For rGO&Ni(OH)$_2$, the characteristic diffraction peaks at 2θ=19.3°, 33.1°, 38.5°, 52.1°, 59.0°, 62.8°, 70.4°, and 73.0° were found, corresponding to the (001), (100), (101), (102), (110), (111), (103), and (201) reflections of β-Ni(OH)$_2$ [43], suggesting Ni(OH)$_2$ was successfully synthesized.

Then, FTIR spectroscopy was carried out (Fig. 2). From the FTIR spectrum of GO, a broad and intensive peak appeared at 3,430 cm^{-1} was assigned to O-H stretching band, which might originate from water molecules adsorbed inside GO. Besides, peaks at 1,726, 1,622, 1,385 and 1,052 cm^{-1} were corresponded to C=O, C=C, C-OH, and C-O-C vibration frequency, respectively. These new peaks suggested that graphite had been already oxidized to GO [44, 45]. However, the FTIR spectrum of rGO showed that the intensities of peaks corresponding to various oxygen-containing functional groups were largely decreased, demonstrating that GO was successfully reduced to rGO. In the FTIR spectrum of rGO&Ni(OH)$_2$, the peaks at 3,642 and 458 cm^{-1} were appeared, which were ascribed to the characteristic peaks of Ni(OH)$_2$, indicating rGO&Ni(OH)$_2$ had been triumphantly obtained.

To further confirm the XRD and FTIR results, Raman spectroscopy and XPS were used to analyze the samples. In the Raman spectra (Fig. 3), both of the curves exhibited two peaks at 1,354 and 1,602 cm^{-1}, corresponding to the D and G bands, respectively. Generally speaking, in the Raman spectrum, the G band represented the in-plane bond-stretching motions of the pairs of C sp^2 atoms (the E_{2g} phonons), while the D band corresponded to the breathing modes of rings or κ-point phonons of A_{1g} symmetry [35]. Thus, the intensity ratio of the D band and G band (I_D/I_G) could be used to roughly estimate the average size of the sp^2 domain of the graphite material. It was found that I_D/I_G value of GO (1.26) was higher than that of rGO (0.93), indicating that the π-conjugated structure from GO was recovered after reduction. Moreover, the I_D/I_G of rGO&Ni(OH)$_2$ was increased to 0.99, which was probably due to the more presences of some unpaired defects
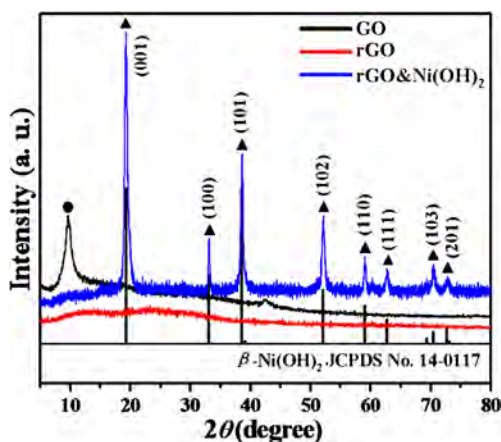
Fig. 1 XRD patterns of GO, rGO, and rGO&Ni(OH)$_2$

and the further decrease in the size of the sp^2 graphitic domain caused by the incorporation of Ni(OH)$_2$ [46]. Nevertheless, the values of I_D/I_G for rGO and rGO&Ni(OH)$_2$ were both much lower than those reported in other study [47] (the values of I_D/I_G for RGO and RGO/Ni(OH)$_2$ were 1.33 and 1.57, respectively), which suggested large size of the sp^2 domain of rGO was retained.

In the XPS survey spectrum of rGO&Ni(OH)$_2$ (Fig. 4a), it showed that the composite mainly consisted of carbon, oxygen, and nickel species. The peak at 284.9 eV was ascribed to the characteristic peak of C 1 s, which could be divided into several peaks (Fig. 4b): C-C (285.0 eV) of sp^2 carbon in the basal plane of rGO, the carbon in C-O (286.6 eV), the carbonyl carbon in C=O (288.4 eV), and the carboxylate carbon in O-C=O (289.3 eV) [48, 49], indicating there were still some residual oxygen-containing groups on the surface of rGO due to the incomplete reduction. Besides, the Ni 2p XPS spectrum (Fig. 4c) showed that two major peaks were centered around 874.4 and 856.8 eV with a spin-energy separation of 17.6 eV, corresponding to Ni 2p$_{1/2}$ and Ni 2p$_{3/2}$, respectively, which were the characteristics of a Ni(OH)$_2$ phase and in good agreement with the previous literature [50]. Remarkably, there
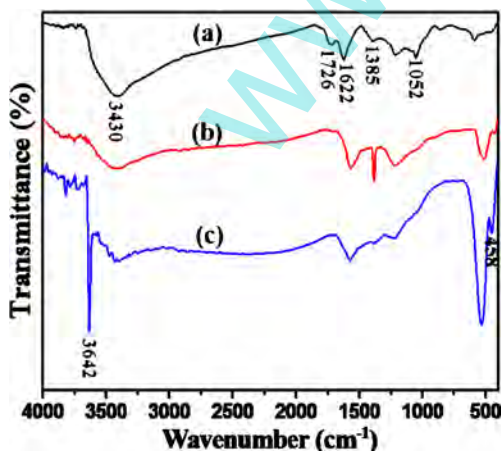

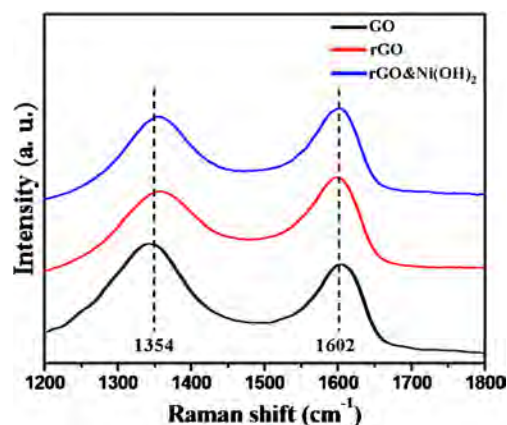**Fig. 2** FTIR spectra of GO (*a*), rGO (*b*), and rGO&Ni(OH)$_2$ (*c*)

**Fig. 3** Raman spectra of GO, rGO, and rGO&Ni(OH)$_2$

were some extra peaks labeled as satellite peaks which were present around the expected Ni 2p$_{1/2}$ and Ni 2p$_{3/2}$ signals in the Ni 2p region.

Furthermore, FESEM image and EDX mapping analysis from a same select area (Fig. 5) also revealed that the composite was primarily composed of elements Ni, C, and O. It could be also seen that element Ni was uniformly distributed, indicating Ni(OH)$_2$ was well distributed on the surface of rGO. Based on the element analysis result (Fig. 6), the contents of elements Ni, C and O were approximately 52.99, 32.62, and 14.39 wt.%, respectively. From the result of calculation, the content of Ni(OH)$_2$ in rGO&Ni(OH)$_2$ was approximately up to 78.87 wt.%. The above results of Raman spectroscopy, XPS, and EDX were consistent with those of XRD and FTIR. In order to further confirm the contents of rGO and Ni(OH)$_2$ in as-prepared rGO&Ni(OH)$_2$, TGA was carried out (Fig. 7). The experiment was performed from 35 to 900 °C in air flow at a heating rate of 10 °C/min. In the process, rGO was burned up, whereas Ni(OH)$_2$ was turned into NiO. The weight loss of rGO&Ni(OH)$_2$ was 38.31 %. On the basis of above analyses, we could conclude that the content of Ni(OH)$_2$ was 76.55 wt.% and the weight ratio of Ni(OH)$_2$ to rGO was derived to be 3.26/1 in rGO&Ni(OH)$_2$, which was consistent with the EDX result.
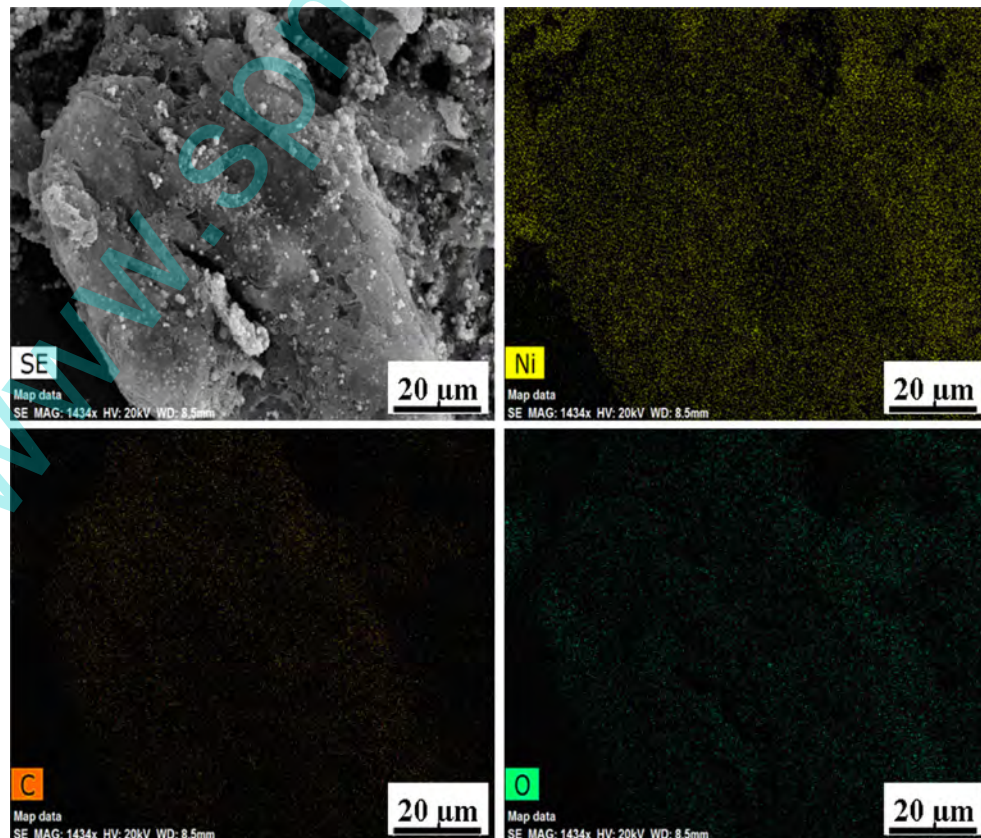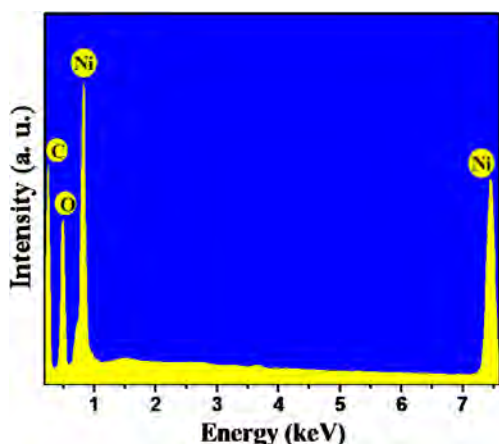
Observation of morphology

Figure 8a showed that the rGO was highly transparent with some visible wrinkles and ripples. In Fig. 8b, the AFM image demonstrated the thickness of rGO was ca. 0.4 nm. Due to the incomplete reduction, the thickness of rGO was a little larger than that of single-layer graphene (0.334 nm). Moreover, the BET data based on nitrogen adsorption and desorption isotherm showed the high surface area of rGO (891.22 m^2/g) (Fig. 8c) that was favorable for loading nanoparticle. The results of TEM, AFM, and BET implied that the obtained rGO nanosheet was few-layer and even single-layer.

Fig. 4 XPS survey spectrum of rGO&Ni(OH)$_2$ (**a**). XPS C 1 s spectrum of rGO&Ni(OH)$_2$ composite (**b**). XPS Ni 2p spectrum of rGO&Ni(OH)$_2$ composite (**c**)
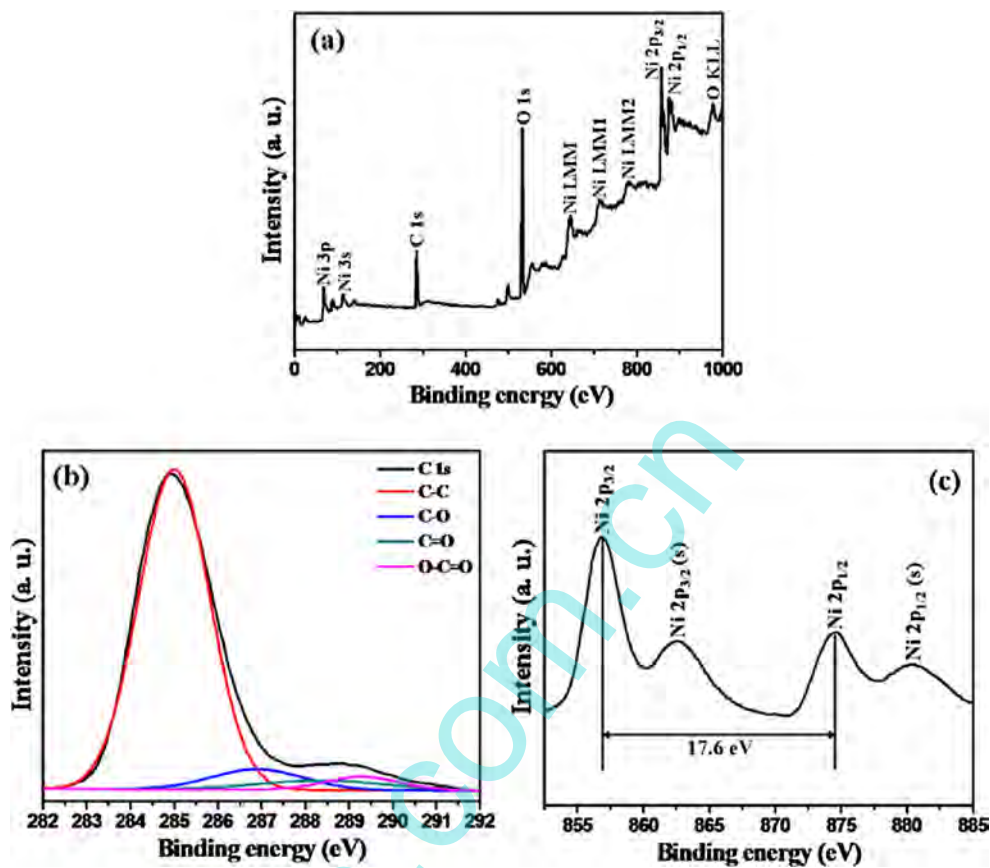
Fig. 5 FESEM image and EDX element mapping analysis of rGO&Ni(OH)$_2$ from the same select area

Fig. 6 EDX characterization of the rGO&Ni(OH)$_2$ composite

On the other hand, the morphology of rGO&Ni(OH)$_2$ composite was investigated by FESEM and TEM. In FESEM images (Figs. 9a, b), it was obviously observed that Ni(OH)$_2$ nanoparticles, which were spherical shapes with diameters of hundreds of nanometers, were well distributed and tightly contacted on the surface of rGO nanosheet. The TEM images (Figs. 9c, d) also showed that the approximately round spots that were ascribed to Ni(OH)$_2$ nanoparticles were closely touched on the surface of rGO nanosheet. Moreover, the black parts of spots might be ascribed to the stacks of Ni(OH)$_2$. Tight contact of Ni(OH)2 and rGO could facilitate for electron transport between Ni(OH)2 and rGO.

Electrochemical properties

To explore the electrochemical performance of rGO&Ni(OH)$_2$, electrochemical measurements were conducted in a three-electrode setup with a platinum counter electrode, a saturated calomel reference electrode, and a 6 mol/L KOH aqueous electrolyte at room temperature.

CV test was generally used to characterize the capacitive behavior of an electrode material. Figure 10a showed the
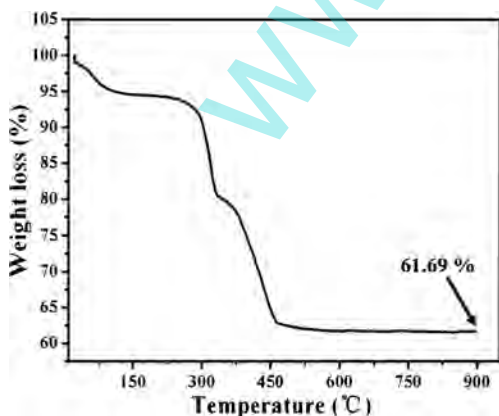
Fig. 7 TGA curve of rGO&Ni(OH)$_2$ performed from 35 to 900 °C in air flow at a heating rate of 10 °C/min

typical CV curves of rGO&Ni(OH)$_2$ at scan rates from 100 to 300 mV/s. Each of the CV curves consisted of a pair of strong redox peaks, and the shapes of CV curves were well distinguished from those of the EDLCs that normally produced CV curves close to ideal rectangular shapes, indicating that the capacitance characteristics were mainly governed by Faradaic redox reaction. The anodic peak (positive current density) occurred around 0.27 V (vs. SCE) indicated an oxidation process related to the oxidation of Ni(OH)$_2$ to NiOOH, while the cathodic peak (negative current density) observed around 0.18 V (vs. SCE) corresponded to the reduction process. For Ni(OH)$_2$ electrode material, it was well accepted that the surface Faradaic reaction would proceed according to the following reaction [2]:

$$Ni(OH)_2 + OH^- \rightleftarrows NiOOH + H_2O + e^- \qquad (1)$$
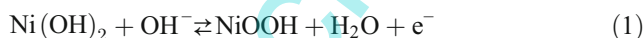
The symmetric characteristic of anodic and cathodic peaks demonstrated the excellent reversibility of rGO&Ni(OH)$_2$ electrode material. More importantly, the shapes of these CV curves almost had no significant change with the scan rate was increased from 100 to 300 mV/s, suggesting improved mass transportation and excellent electron conduction. It should be also noted that slight shifts of oxidation peaks and reduction peaks were found, which were probably caused by the internal resistance of electrode.

To discuss more detailedly, GCD measurements were carried out to study the electrochemical property of rGO&Ni(OH)$_2$. The GCD curves performed at various current densities were given in Fig. 10b. Generally, the specific capacitance (C_s, F/g) could be calculated by the following equation:

$$C_s = \frac{It}{m\Delta V} \qquad (2)$$

where I was the discharge current (A), t was the time for a full discharge (s), m was the mass of electroactive material (g), and ΔV was the potential range of a full discharge (V). From the results of calculation based on the mass of rGO&Ni(OH)$_2$ (Fig. 10f), the highest C_s value of 1,576 F/g at current density of 6 A/g was obtained. With the increase of current density, the C_s of rGO&Ni(OH)$_2$ was gradually decreased, which might be because some parts of the surface of rGO&Ni(OH)$_2$ were inaccessible at high charge and discharge rate. However, it was worthy noting that the decay of C_s was not greatly obvious. Even though the current density was increased to 42 A/g, rGO&Ni(OH)$_2$ still presented pretty high C_s value (1,008 F/g). For comparison, the GCD measurements of rGO and Ni(OH)$_2$ were also performed. Figure 10e displayed the discharge curves of rGO, Ni(OH)$_2$, and rGO&Ni(OH)$_2$ at a current density of 6 A/g. Since the C_s was proportional to the time for a full discharge

Fig. 8 TEM image of rGO (**a**). Tapping-mode AFM image of rGO on a clean mica surface and cross-sectional profile of rGO indicated by a blue line (**b**). Nitrogen adsorption and desorption isotherm for rGO (**c**)
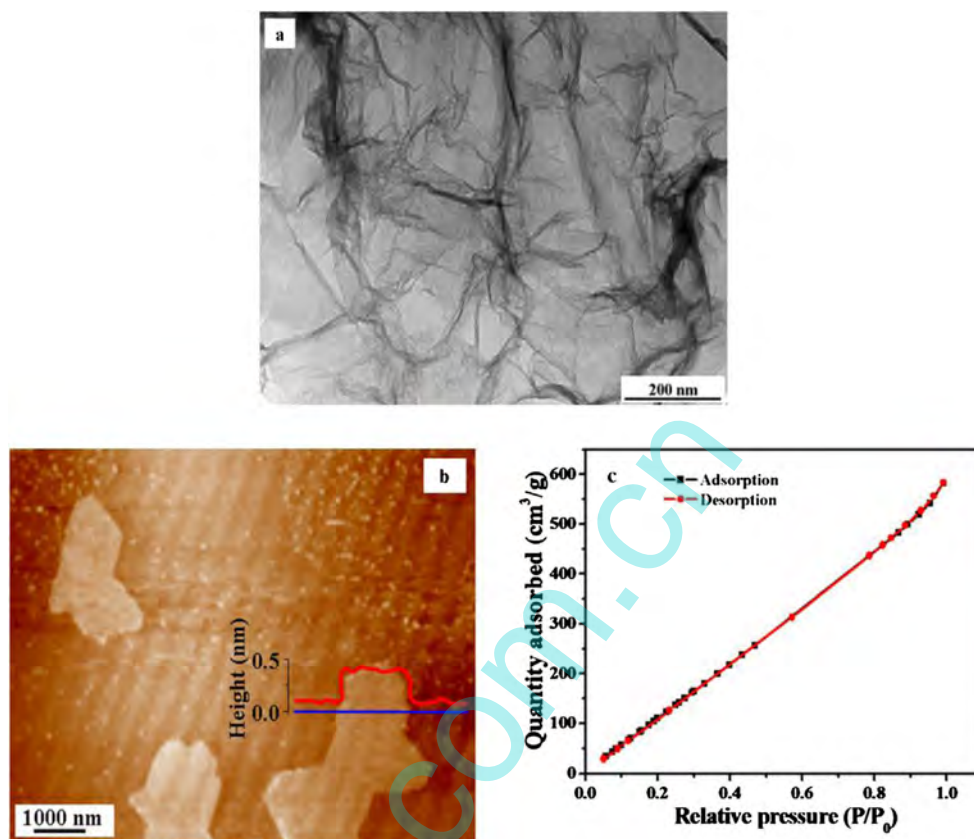

(Eq. (2)), it was obvious that the C_s of rGO&Ni(OH)$_2$ was superior to that of rGO or Ni(OH)$_2$. Besides, Fig. 10f presented the relationship between C_s and current density of rGO, Ni(OH)$_2$, and rGO&Ni(OH)$_2$. Obviously, the C_s value of rGO&Ni(OH)$_2$ was higher than that of rGO or Ni(OH)$_2$ at every testing point. In addition, approximate

64 % (1,008 F/g) of the initial capacitance (1,576 F/g) for rGO&Ni(OH)$_2$ was retained when the current density increased from 6 to 42 A/g. However, rGO and Ni(OH)$_2$ reserved only 54 % (from 208 to 112 F/g) and 46 % (from 612 to 280 F/g), respectively. The higher capacitance and larger retention ratio of rGO&Ni(OH)$_2$ could be attributed

Fig. 9 FESEM images (**a**, **b**) and TEM images (**c**, **d**) of rGO&Ni(OH)$_2$
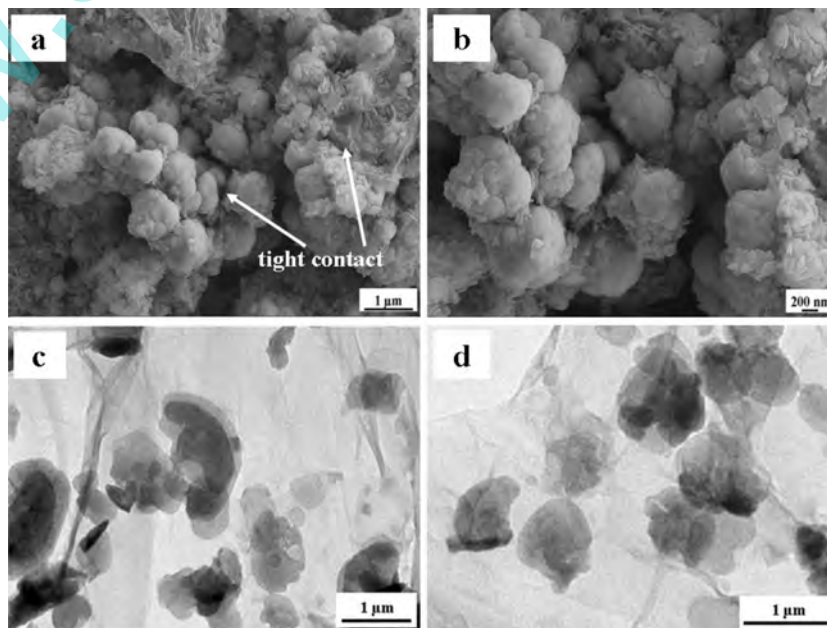
Fig. 10 CV curves for
rGO&Ni(OH)$_2$ electrode at
different scan rates (**a**). GCD
curves of rGO&Ni(OH)$_2$
electrode collected at different
current densities (**b**). Nyquist plot
of rGO&Ni(OH)$_2$ electrode.
Inset: The data of Nyquist plot of
rGO&Ni(OH)$_2$ electrode at high-
frequency range (**c**). Ragone plot
of energy density vs. power
density for rGO&Ni(OH)$_2$
electrode (**d**). Discharge curves of
rGO, Ni(OH)$_2$, and
rGO&Ni(OH)$_2$ at a current
density of 6 A/g (**e**). C_s of rGO,
Ni(OH)$_2$, and rGO&Ni(OH)$_2$
electrodes measured as a function
of current density (**f**). Cycle
performances of rGO, Ni(OH)$_2$,
and rGO&Ni(OH)$_2$ electrodes
measured at a current density of
6 A/g (**g**)
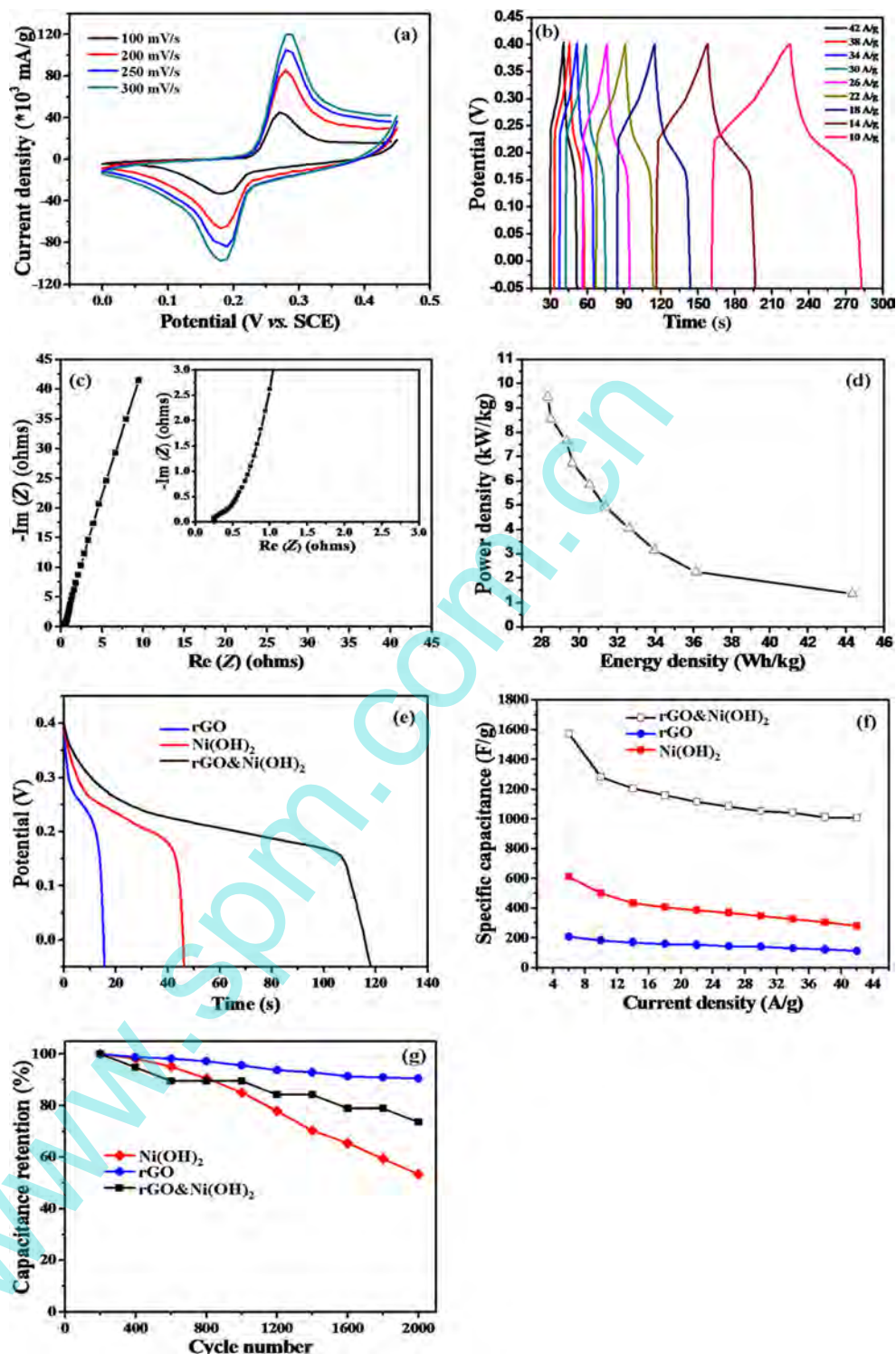
to the synergistic contribution of electrochemical double-layer capacitance of rGO and pseudocapacitance of Ni(OH)$_2$. Remarkably, as shown in Table 1, the C_s of rGO&Ni(OH)$_2$ in this paper was highly comparable with and even much higher than those of composites based on graphene and Ni(OH)$_2$ in other studies [2, 47, 50–53],

those of composites based on Ni(OH)$_2$ and other materials [54–56], and those of other transition metal oxides or their composites [12, 23–26].

Moreover, the cycle life was tested by repeating GCD tests at a current density of 6 A/g. The results (Fig. 10g) exhibited cycle stabilities of rGO, Ni(OH)$_2$, and rGO&Ni(OH)$_2$

Table 1 Summary of electrochemical data of some electrode materials. Complete data can be found in the related literatures

Sample	Method	C_s (F/g)	Electrolyte	Potential window (V)	Current density or scan rate	Reference
RGO/Ni(OH)$_2$	Hydrothermal	780	1 M KOH	0.50	10 A/g	[47]
Ni(OH)$_2$/graphene	Hydrothermal	953	1 M KOH	0.50	45.7 A/g	[2]
Ni(OH)$_2$/graphene	Microwave heating	523	6 M KOH	0.55	50 mV/s	[51]
Graphene/Ni(OH)$_2$	Solid-state reaction	820	1 M KOH	0.60	4 A/g	[52]
Ni(OH)$_2$/graphene	Chemical precipitation	895	6 M KOH	0.55	20 mV/s	[53]
rGO/Ni(OH)$_2$	Non-aqueous approach	428	6 M KOH	0.45	100 mV/s	[50]
Ni(OH)$_2$/ZnO	Hydrothermal	982.5	1 M KOH	0.55	39.3 A/g	[54]
Ni(OH)$_2$/CNTs	Hydrothermal	771.3	6 M KOH	0.50	20 A/g	[55]
Ni(OH)$_2$/CNTs	Chemical precipitation	118	6 M KOH	0.50	500 mV/s	[56]
RuO$_2$	Anodic deposition	780	1 M H$_2$SO$_4$	1.00	1,000 mV/s	[23]
Co$_3$O$_4$	Electrodeposition	885.7	5 M NaOH	0.63	20 A/g	[24]
NiO	Hydrothermal	283.5	2 M KOH	0.50	10 A/g	[25]
Fe$_2$O$_3$	Anodization	91	1 M Li$_2$SO$_4$	0.80	12.8 A/g	[26]
MnO$_2$/ZnO	Self-limiting process	740.9	0.5 M Na$_2$SO$_4$	0.80	45.5 A/g	[12]
rGO&Ni(OH)$_2$	Chemical precipitation	1,008	6 M KOH	0.45	42 A/g	This work

electrode material maintaining 90, 53, and 74 % of its specific capacitance after 2,000 cycles, respectively. Compared with rGO, the worse cycle life of rGO&Ni(OH)$_2$ was probably attributed to the phase transformation or the growth of particle and crystal size of the electrode material during the rapid charge and discharge process in alkali solution [57]. However, rGO&Ni(OH)$_2$ displayed better cycle life than Ni(OH)$_2$, which was ascribed to the positive interaction between rGO and Ni(OH)$_2$. On the other hand, the ability of electrode material to retain high C_s at high discharge rate usually contributed to prominent energy and power characteristics. Ragone plot relating the energy density to power density was an efficient way to evaluate the capacitive performance of electrode material. The energy density (E, Wh/kg) and power density (P, W/kg) could be obtained from the following formulas [4]:

$$E = \frac{1}{2} C_s (\Delta V)^2 \tag{3}$$

$$P = \frac{E}{t} \tag{4}$$

where C_s, ΔV, and t were indicating the specific capacitance (F/g), the potential range of a full discharge (V) and the time for a full discharge (s), respectively. Figure 10d showed the Ragone plot of rGO&Ni(OH)$_2$ derived from the GCD curves at different current densities. The rGO&Ni(OH)$_2$ electrode displayed a good energy density of 44.32 Wh/kg at a power density of 1,350 W/kg, and an energy density of 28.35 Wh/kg could be still retained even if the power density was increased to 9,450 W/kg, which was thanks to the good rate capability of

rGO&Ni(OH)$_2$, suggesting the rGO&Ni(OH)$_2$ was a highly promising candidate as electrode material for practical applications in SCs. The electrochemical testing results mentioned above all proved that the rGO&Ni(OH)$_2$ electrode material had significantly excellent electrochemical properties, including high capacitance, good rate capability, excellent stability, long cycle life, etc.

Exploration of mechanism

From the above analyses, the mechanism for excellent electrochemical performance of rGO&Ni(OH)$_2$ was suggested as follows (Fig. 11). (CH$_2$)$_6$N$_4$ could gradually generate NH$_3$ through decomposition when it was heated [58]. While (CH$_2$)$_6$N$_4$ was mixed with GO under the condition of heating, many NH$_3$ molecules were inserted into the interlayer of GO. During the reduction process at higher temperature, the equilibrium of system was disturbed since the structure of GO began to change and the Ni(OH)$_2$ was gradually generated, resulting the beforehand-accumulated NH$_3$ molecules were released. Such abundant releases of gases would be favored for effectively protecting rGO from agglomeration and restacking during the reduction process, causing the few-layer rGO nanosheet with high BET surface area that could supply large available contact area for nanoparticle (Figs. 1 and 8).

On the other hand, generally speaking, in order to prevent graphene from agglomeration, stabilizers [47] or modifiers [52] were usually introduced. However, either of them was difficult to be removed, which might influence the transportation and migration of electron, leading to the decline in the

Fig. 11 Schematic of synthesis of rGO&Ni(OH)$_2$

●O ○OH ○COOH ▭NH$_3$ ◯Ni(OH)$_2$
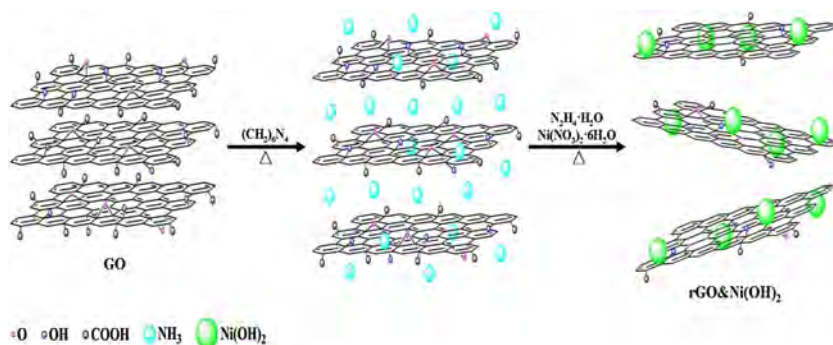
excellent property of graphene. Nevertheless, the element N was not detected in rGO&Ni(OH)$_2$ (Figs. 4, 5, and 6), so we could know that the NH$_3$ was not only acted as the pre-stabilizer, but also easy to be removed. Thanks to no residual of pre-stabilizer of NH$_3$ and effective prevention of agglomeration and re-stacking of rGO with large size of the sp^2 domain (Figs. 1, 2, 3, 4, 5, 6, and 8), few-layer rGO nanosheet could act as support which was favored for the rapid transport and migration of electrolyte ion and electron. After the incorporation of Ni(OH)$_2$ nanoparticle, the rGO and Ni(OH)$_2$ were tightly contacted (Fig. 9) which facilitated for electron transport between Ni(OH)2 and rGO, resulting the weakness of low conductivity of Ni(OH)$_2$ was immensely overcome. To understand the electrochemical conductivity behavior of rGO&Ni(OH)$_2$, the EIS data were analyzed using Nyquist plot. In Fig. 10c, the Nyquist plot of rGO&Ni(OH)$_2$ started with a semicircle loop followed by a rising along imaginary impedance axis. It could be seen that the semicircle loop was not obvious, implying fast charge transfer of rGO&Ni(OH)$_2$. Then, the line featured a quite vertical curve, demonstrating fast diffusion process and nearly ideal capacitive behavior of rGO&Ni(OH)$_2$.

All these results supported that the rGO&Ni(OH)$_2$ had excellent electrochemical performance. The reasons could be discussed as follows. First, the agglomeration and re-stacking of rGO could be effectively prevented by pre-stabilizer of NH$_3$ that could be easily removed, leading to the formation of few-layer rGO nanosheet which was beneficial for the rapid transport and migration of electrolyte ion and electron. Second, few-layer rGO exhibited high specific surface area which provided many available contact areas for load of nanoparicle. Third, the rGO in the composite could significantly buffer the volume change of Ni(OH)$_2$ during the rapid charge/discharge process, which was favored for good cycling performance. Finally, Ni(OH)$_2$ nanoparticle was touched tightly on the surface of rGO nanosheet, which could remarkably enhance the electrochemical utilization of Ni(OH)$_2$ because of the shortened length of electron transport and migration. In a conclusion, facile process and excellent electrochemical property signified the great potential application of rGO&Ni(OH)$_2$ in SCs.

Conclusion

Pre-stabilized rGO by NH$_3$ was served as carrier for Ni(OH)$_2$ with an easy process. The NH$_3$ could effectively protect rGO from agglomeration and re-stacking and could be easily removed which was quite different from other stabilizers or modifiers. The results showed that the obtained few-layer rGO nanosheet exhibited high BET surface area of 891.22 m^2/g that was favorable for load of nanoparticle. After the combination of Ni(OH)$_2$ nanoparticle, rGO&Ni(OH)$_2$ composite had excellent electrochemical property thanks to effective prevention of agglomeration and re-stacking of rGO with large size of the sp^2 domain, no residual of pre-stabilizer of NH$_3$, and tight contact between rGO and Ni(OH)$_2$. The electrochemical tests indicated rGO&Ni(OH)$_2$ electrode exhibited excellent stability at scan rates from 100 to 300 mV/s. A high specific capacitance of 1,008 F/g could be obtained at high current density of 42 A/g in 6 mol/L KOH aqueous solution. With the current density was increased from 6 to 42 A/g, the specific capacitance had low decay of 36 % (from 1,576 to 1,008 F/g), revealing good rate capability. A good energy density of 44.32 Wh/kg had been obtained at a power density of 1,350 W/kg and an energy density of 28.35 Wh/kg could be still retained when the power density was increased to 9,450 W/kg. Moreover, the rGO&Ni(OH)$_2$ electrode showed a long cycle life, retaining 74 % specific capacitance after 2,000 cycles at current density of 6 A/g. Excellent overall performance and facile process indicated such composite would be a highly promising candidate as electrode material for broad application in energy conversion/storage system.

References

1. Simon P, Gogotsi Y (2008) Nat Mater 7:845–854
2. Wang HL, Casalongue HS, Liang YY, Dai HJ (2010) J Am Chem Soc 132:7472–7477
3. Chen Z, Qin YC, Weng D, Xiao QF, Peng YT, Wang XL, Li HX, Wei F, Lu YF (2009) Adv Funct Mater 19:3420–3426
4. Fan ZJ, Yan J, Wei T, Zhi LJ, Ning GQ, Li TY, Wei F (2011) Adv Funct Mater 21:2366–2375
5. Bao LH, Zang JF, Li XD (2011) Nano Lett 11:1215–1220
6. Chen Z, Augustyn V, Wen J, Zhang YW, Shen MQ, Dunn B, Lu YF (2011) Adv Mater 23:791–795
7. Ghosh A, Lee YH (2012) ChemSusChem 5:480–499
8. Zhang LL, Zhao XS (2009) Chem Soc Rev 38:2520–2531
9. Liu C, Li F, Ma LP, Cheng HM (2010) Adv Mater 22:E28–E62
10. Jiang H, Yang LP, Li CZ, Yan CY, Lee PS, Ma J (2011) Energy Environ Sci 4:1813–1819
11. Conway BE (1999) Electrochemical supercapacitors: scientific fundamentals and technological applications. Kluwer Academic/Plenum Publisher, New York
12. Yang PH, Xiao X, Li YZ, Ding Y, Qiang PF, Tan XH, Mai WJ, Lin ZY, Wu WZ, Li TQ, Jin HY, Liu PY, Zhou J, Wong CP, Wang ZL (2013) ACS Nano 7:2617–2626
13. Epifani M, Chavez-Capilla T, Andreu T, Arbiol J, Palma J, Morante JR, Diaz R (2012) Energy Environ Sci 5:7555–7558
14. Jiang J, Li YY, Liu JP, Huang XT, Yuan CZ, Lou XW (2012) Adv Mater 24:5166–5180
15. Jiang H, Ma J, Li CZ (2012) Adv Mater 24:4197–4202
16. Lu XH, Yu MH, Zhai T, Wang GM, Xie SL, Liu TY, Liang CL, Tong YX, Li Y (2013) Nano Lett 13:2628–2633
17. Mai LQ, Yang F, Zhao YL, Xu X, Xu L, Luo YZ (2011) Nat Commun 2. doi:10.1038/ncomms1387
18. Dai SG, Xi Y, Hu CG, Liu JL, Zhang KY, Yue XL, Cheng L (2013) J Mater Chem A 1:15530–15534
19. Frackowiak E (2007) Phys Chem Chem Phys 9:1774–1785
20. Zhai YP, Dou YQ, Zhao DY, Fulvio PF, Mayes RT, Dai S (2011) Adv Mater 23:4828–4850
21. Stoller MD, Park SJ, Zhu YW, An JH, Ruoff RS (2008) Nano Lett 8:3498–3502
22. Zhu YW, Murali S, Stoller MD, Ganesh KJ, Cai WW, Ferreira PJ, Pirkle A, Wallace RM, Cychosz KA, Thommes M, Su D, Stach EA, Ruoff RS (2011) Science 332:1537–1541
23. Hu CC, Chang KH, Lin MC, Wu YT (2006) Nano Lett 6:2690–2695
24. Kung CW, Chen HW, Lin CY, Vittal R, Ho KC (2012) J Power Sources 214:91–99
25. Wang B, Chen JS, Wang ZY, Madhavi S, Lou XW (2012) Adv Energy Mater 2:1188–1192
26. Xie KY, Li J, Lai YQ, Lu W, Zhang ZA, Liu YX, Zhou LM, Huang HT (2011) Electrochem Commun 13:657–660
27. Lu XH, Zheng DZ, Zhai T, Liu ZQ, Huang YY, Xie SL, Tong YX (2011) Energy Environ Sci 4:2915–2921
28. Li HB, Yu MH, Wang FX, Liu P, Liang Y, Xiao J, Wang CX, Tong YX, Yang GW (2013) Nat Commun 4. doi:10.1038/ncomms2932
29. Jiang H, Lee PS, Li CZ (2013) Energy Environ Sci 6:41–53
30. Candelaria SL, Shao YY, Zhou W, Li XL, Xiao J, Zhang JG, Wang Y, Liu J, Li JH, Cao GZ (2012) Nano Energy 1:195–220
31. Wu Q, Xu YX, Yao ZY, Liu AR, Shi GQ (2010) ACS Nano 4:1963–1970
32. Xu JJ, Wang K, Zu SZ, Han BH, Wei ZX (2010) ACS Nano 4:5019–5026
33. Qu QT, Yang SB, Feng XL (2011) Adv Mater 23:5574–5580
34. Yu GH, Hu LB, Vosgueritchian M, Wang HL, Xie X, McDonough JR, Cui X, Cui Y, Bao ZN (2011) Nano Lett 11:2905–2911
35. Yan J, Wei T, Shao B, Fan ZJ, Qian WZ, Zhang ML, Wei F (2010) Carbon 48:487–493
36. Yan J, Wei T, Fan ZJ, Qian WZ, Zhang ML, Shen XD, Wei F (2010) J Power Sources 195:3041–3045
37. Ji JY, Zhang LL, Ji HX, Li Y, Zhao X, Bai X, Fan XB, Zhang FB, Ruoff RS (2013) ACS Nano 7:6237–6243
38. Shahid M, Liu JL, Shakir I, Warsi MF, Nadeem M, Kwon YU (2012) Electrochim Acta 85:243–247
39. Chen G, Liaw SS, Li BS, Xu Y, Dunwell M, Deng SG, Fan HY, Luo HM (2014) J Power Sources 251:338–343
40. Liu JP, Jiang J, Cheng CW, Li HX, Zhang JX, Gong H, Fan HJ (2011) Adv Mater 23:2076–2081
41. Hummers WS, Offeman RE (1958) J Am Chem Soc 80:1339–1341
42. Kovtyukhova NI, Ollivier PJ, Martin BR, Mallouk TE, Chizhik SA, Buzaneva EV, Gorchinskiy AD (1999) Chem Mater 11:771–778
43. Li BJ, Cao HQ, Shao J, Zheng H, Lu YX, Yin JF, Qu MZ (2011) Chem Commun 47:3159–3161
44. Jeong HK, Lee YP, Lahaye RJWE, Park MH, An KH, Kim IJ, Yang CW, Park CY, Ruoff RS, Lee YH (2008) J Am Chem Soc 130:1362–1366
45. Guo HL, Wang XF, Qian QY, Wang FB, Xia XH (2009) ACS Nano 3:2653–2659
46. Tuinstra F, Koenig JL (1970) J Chem Phys 53:1126–1130
47. Chang J, Xu H, Sun J, Gao L (2012) J Mater Chem 22:11146–11150
48. Datsyuk V, Kalyva M, Papagelis K, Parthenios J, Tasis D, Siokou A, Kallitsis I, Galiotis C (2008) Carbon 46:833–840
49. Park S, An JH, Jung IW, Piner RD, An SJ, Li XS, Velamakanni A (2009) Nano Lett 9:1593–1597
50. Lee JW, Ahn T, Soundararajan D, Ko JM, Kim JD (2011) Chem Commun 47:6305–6307
51. Yan J, Fan ZJ, Sun W, Ning GQ, Wei T, Zhang Q, Zhang RF, Zhi LJ, Wei F (2012) Adv Funct Mater 22:2632–2641
52. Sun ZP, Lu XM (2012) Ind Eng Chem Res 51:9973–9979
53. Yan J, Sun W, Wei T, Zhang Q, Fan Z, Wei F (2012) J Mater Chem 22:11494–11502
54. Liu JP, Cheng CW, Zhou WW, Li HX, Fan HJ (2011) Chem Commun 47:3436–3438
55. Chen S, Zhu JW, Zhou H, Wang X (2011) RSC Adv 1:484–489
56. Liu CG, Lee YS, Kim YJ, Song IC, Kim JH (2009) Synth Met 159:2009–2012
57. Hu GX, Li CX, Gong H (2010) J Power Sources 195:6977–6981
58. Liang ZW, Cui H, Wang K, Yang PH, Zhang L, Mai WJ, Wang CX, Liu PY (2012) CrystEngComm 14:1723–1728